Micron 116 (2019) 22–29

Contents lists available at ScienceDirect

Micron

journal homepage: www.elsevier.com/locate/micron

Dynamic behavior of nanoscale liquids in graphene liquid cells revealed by *in situ* transmission electron microscopy

Jiwoong Yang[a], Sardar B. Alam[a], Lei Yu[a,c], Emory Chan[b], Haimei Zheng[a,c,*]

[a] Materials Sciences Division, Lawrence Berkeley National Laboratory, Berkeley, CA 94720, United States
[b] The Molecular Foundry, Lawrence Berkeley National Laboratory, Berkeley, CA 94720, United States
[c] Department of Materials Science and Engineering, University of California, Berkeley, CA 94720, United States

ARTICLE INFO

Keywords:
Liquid cell TEM
In situ TEM
Graphene liquid cells
Nanoscale
Liquid dynamics
Solid-liquid-gas interfaces

ABSTRACT

Recent advances in graphene liquid cells for *in situ* transmission electron microscopy (TEM) have opened many opportunities for the study of materials transformations and chemical reactions in liquids with high spatial resolution. However, the behavior of thin liquids encapsulated in a graphene liquid cell has not been fully understood. Here, we report real time TEM imaging of the nanoscale dynamic behavior of liquids in graphene nanocapillaries. Our observations reveal that the interfaces between liquid and gas bubble can fluctuate, leading to the generation of liquid nanodroplets near the interfaces. Liquid nanodroplets often show irregular shape with dynamic changes of their configuration under the electron beam. We consider that the dynamic motion of liquid-gas interfaces might be introduced by the electrostatic energy from transiently charged interfaces. We find that improving the wettability of graphene liquid cells by ultraviolet-ozone treatment can significantly modify the dynamic motion of the encapsulated liquids. Our study provides valuable information of the interactions between liquid and graphene under the electron beam, and it also offers key insights on the nanoscale fluid dynamics in confined spaces.

1. Introduction

Liquid cell transmission electron microscopy (TEM) enables the direct observation of dynamic phenomena in liquids, including electrochemical reactions, crystal growth, and the activity of biological materials in their native environment. The high spatial and temporal resolution afforded by this emerging imaging modality is not achievable with other characterization tools (de Jonge and Ross, 2011; Ross, 2015; Zhu and Durr, 2015; Liao and Zheng, 2016; De Yoreo and Sommerdijk, 2016). Examples of implementation of this technique can be found in the *in situ* imaging of nucleation and growth of nanocrystals (Zheng et al., 2009; Nielsen et al., 2014; Woehl et al., 2012; Lee et al., 2016; Sutter et al., 2017), nanoparticle self-assembly (Powers et al., 2016; Luo et al., 2017; Tan et al., 2017), materials transformations and nanocrystal shape evolution (Liao et al., 2014; Niu et al., 2014; Sutter et al., 2014; Jiang et al., 2017), electrochemical process (Williamson et al., 2003; Gu et al., 2013; Zhang et al., 2017; Zeng et al., 2017; Song and Xie, 2018), and biological samples (Park et al., 2015a; Dahmke et al., 2017). Technically, liquid cells separating the liquid samples from the high vacuum environment of TEM allow imaging with the general workflow of conventional TEM. The development of liquid cell TEM has benefited from the advances of both TEM instruments and liquid cell fabrication (Ross, 2015; Kim et al., 2018). Graphene can encapsulate thin pockets of liquids with thicknesses of tens of nanometers (Yuk et al., 2012). Since graphene is highly transparent to the electron beam, the electron beam scattering by the window materials and small volume of liquid solution is minimized, hence the spatial resolution using graphene liquids has been significantly improved (Yuk et al., 2012; Park et al., 2015b; Kelly et al., 2018; Textor and de Jonge, 2018; de Jonge, 2018). To comprehend the phenomena that take place during liquid cell TEM experiments, the fundamental understanding of nanoscale liquid dynamics under the electron beam is essential (Abellan et al., 2014; Niu et al., 2015; Zhou et al., 2017). Previously, the unique behavior of water nanodroplets on hydrophilic SiN_x membrane has been captured using liquid cell TEM (Mirsaidov et al., 2012; Bhattacharya et al., 2014; Leong et al., 2014). However, our understanding of the nanoscale liquid dynamics in graphene liquid cells is still limited. In the earlier studies, graphene has been regarded as inert (Yuk et al., 2012; Chen et al., 2013), but a recent study demonstrated that graphene can act as a radical scavenger during TEM measurements using graphene liquid cells (Cho et al., 2017). Considering the active properties and the applications of graphene as a unique substrate for various nanomaterials (Geim

* Corresponding author at: Materials Sciences Division, Lawrence Berkeley National Laboratory, Berkeley, CA 94720, United States.
E-mail address: hmzheng@lbl.gov (H. Zheng).

https://doi.org/10.1016/j.micron.2018.09.009
Received 1 August 2018; Received in revised form 10 September 2018; Accepted 14 September 2018
Available online 17 September 2018
0968-4328/

and Grigorieva, 2013; Novoselov et al., 2016; Lee et al., 2015; Choi et al., 2015; Wang et al., 2015; Yang et al., 2017), graphene-liquid interactions cannot be neglected for studies using graphene liquid cells.

From another point of view, nanoscale confined liquids have gained a great deal of interest because of their unique properties (Holt et al., 2006; Takaiwa et al., 2008; Li et al., 2014) and their potential applications in nanofluidic devices and biological processes (Lucent et al., 2007; Kim et al., 2015; Cohen-Tanugi et al., 2016). Investigating the dynamic behavior of confined nanoscale liquids has been a great challenge due to the lack of effective experimental techniques for characterizing their dynamics (Kolesnikov et al., 2004; Song et al., 2014; Dollekamp et al., 2017). Therefore, many of the previous works are based on computational approaches such as molecular dynamics (Pestana et al., 2018) and first principle studies (Cicero et al., 2008; Chen et al., 2016). A recent experimental study of nanoscale water confined between graphene sheets suggested a unique structure of liquid (Algara-Siller et al., 2015), however, there are currently considerable debates on this topic (Zhou et al., 2015; Chen et al., 2016).

Herein we present an *in situ* TEM study of the dynamic behavior of aqueous solution encapsulated between two graphene sheets in a graphene liquid cell. The bubble formation and nanoscale fluctuations of liquid-gas interfaces are observed. We find that the dynamic motion of interfaces can lead to the formation of liquid nanodroplets near the interface and inside the gas bubbles. These liquid nanodroplets often show irregular shape with dynamic changes. We show that improving the wettability of graphene liquid cells through ultraviolet-ozone treatment has drastic effects on the dynamic behavior of liquid. This study facilitates fundamental understanding of nanoscale liquid dynamics during liquid cell TEM measurements, and it demonstrates *in situ* liquid cell TEM as a promising tool for studying nanofluidics.

2. Experimental methods

2.1. Fabrication of graphene liquid cells

Graphene liquid cells containing aqueous solutions were prepared by encapsulating each solution between a pair of graphene-coated TEM grids. First, multilayer graphene sheets on copper foil were transferred to Quantifoil film TEM grids (Ted Pella Inc., US) by the modified direct wet transfer method (Regan et al., 2010). Specifically, multilayer graphene sheets ($\sim 3-5$ layers, ACS Materials, US) synthesized by chemical vapor deposition on copper foils were used in this study. Quantifoil carbon film TEM grids were placed on top of multilayer graphene on copper foils. Several drops of isopropanol (> 99.5%, Sigma-Aldrich, US) were introduced between the Quantifoil carbon films and graphene sheets and dried under mild heating (80 °C) to enhance the adhesion of graphene to the TEM grids. The copper substrate was etched by sodium persulfate (< 98%, Sigma-Aldrich) solution (50 mg/ml in Milli-Q water) for ~8 h to completely remove copper from the surface of graphene. The resulting graphene-coated TEM grids were mildly washed with Milli-Q water at least three times. Finally, graphene liquid cells were obtained by encapsulating the aqueous solution between a pair of graphene-coated TEM grids. The aqueous solution was prepared by dissolving NaCl in Milli-Q water (~3 wt%). The addition of salt is expected to result in the increase of surface tension, which decreases the wettability of the water solution on hydrophobic surfaces (Zisman, 1964; Nayar et al., 2014). The relation between the wettability and the liquid dynamics is discussed in the Section 3.3. A small amount of the solution (< 0.1 μL) was placed on the graphene side of the as-prepared graphene-coated TEM grid. Another graphene-coated TEM grid was placed onto the liquid solution dispensed on the first TEM grid and the excess solution squeezed out was removed by a piece of filter paper. The top and bottom TEM grids were held together by tweezers for more than one hour, which resulted in the formation of many isolated liquid pockets in the graphene liquid cell.

Comparison experiments were performed using surface modified graphene liquid cells. The ultraviolet-ozone (UVO) treatment was conducted using a Jelight UVO-Cleaner® Model 42. Graphene-coated TEM grids were treated by UVO for various exposure times (30, 90, 150, 300, and 600 s) before the fabrication of liquid cells.

2.2. TEM analysis

The graphene liquid cells were characterized by a JEOL JEM-2100 transmission electron microscope with a high-resolution pole piece, a LaB_6 filament and a Gatan Orius SC200 CCD camera. The operating voltage of TEM was 200 kV. The electron dose rate was controlled ($100-500\ e^-/Å^2\,s$) to limit bubble generation which can interrupt experiments. *In situ* TEM movies were acquired at 2–5 frames per second; the frame rate for each movie is indicated in the supplementary information. For all the movies in the supplementary information, the playback speed is 4 times faster than their original speed. Movies were compressed into MP4 format for publication, but the original data were used for the data analysis. Area, center of the mass, and circularity of the objects of interest were analyzed by FIJI software (Schindelin et al., 2012). The circularity is defined as, circularity $= 4\pi \times \text{area/perimeter}^2$. The value is 1.0 for a perfect circle and is decreasing as a boundary become irregular or shape elongates.

Electron energy loss spectroscopy (EELS) analysis was performed using a monochromated FEI Tecnai F20 UT operated at 200 kV at the National Center for Electron Microscopy within the Molecular Foundry in Lawrence Berkeley National Laboratory. The microscope is equipped with a Tridiem Gatan imaging filter and a double-focusing Wien filter acting as a monochromator below the field-emission gun. The spectra were acquired with an energy dispersion of 0.1 eV/channel and with an exposure time of ~4 s.

2.3. Other characterization methods

Raman spectra of graphene-coated grids were acquired by a Horiba Jobin Yvon LabRAM ARAMIS automated scanning confocal Raman microscope under the excitation of a 532 nm laser. The contact angle of pure water on graphene-coated grids was measured using a Ramé-Hart contact angle goniometer. Small drops (*ca.* 0.5 μL) of Mili-Q water were used for the measurements. The obtained images were analyzed by FIJI software (Schindelin et al., 2012) with a contact angle plug-in (Stalder et al., 2006). The final values were averaged from five measurements for each experimental condition.

3. Results and discussion

3.1. Dynamics of liquid-gas interfaces and nanodroplet formation

We characterize the aqueous solution encapsulated in graphene liquid cells using TEM operated at 200 kV. *In situ* observation reveals the dynamic behavior of the nanoscale liquid between two graphene sheets (Movie S1 and S2). The schematic illustration of the overall process is described in Fig. 1(a), and the representative images from each movie are captured and displayed in Fig. 1(b) and (c). The dark and bright parts in TEM images are liquid and gas (or dried regions), respectively, while the thickness of the liquid in graphene liquid cells is estimated to be in the range of tens of nanometers (Yuk et al., 2012). The liquid-gas interface is highlighted with dashed lines and their contour plots for each movie are displayed in Fig. 1(d) and (e). Gas bubbles in graphene liquid cells are observed at the initial stage (Fig. 1(a)–(c)), and their sizes range from several nanometers to micrometers. These gas bubbles are known to be originating from either the water radiolysis by the electron beam (Schneider et al., 2014; Grogan et al., 2014) or from the evolution of external gas originally dissolved in the encapsulated liquid. It is also suggested that these gases are byproducts of the oxidation of graphene which acts as a radical scavenger (Cho et al., 2017). We note that aqueous solutions in graphene liquid cells can easily produce

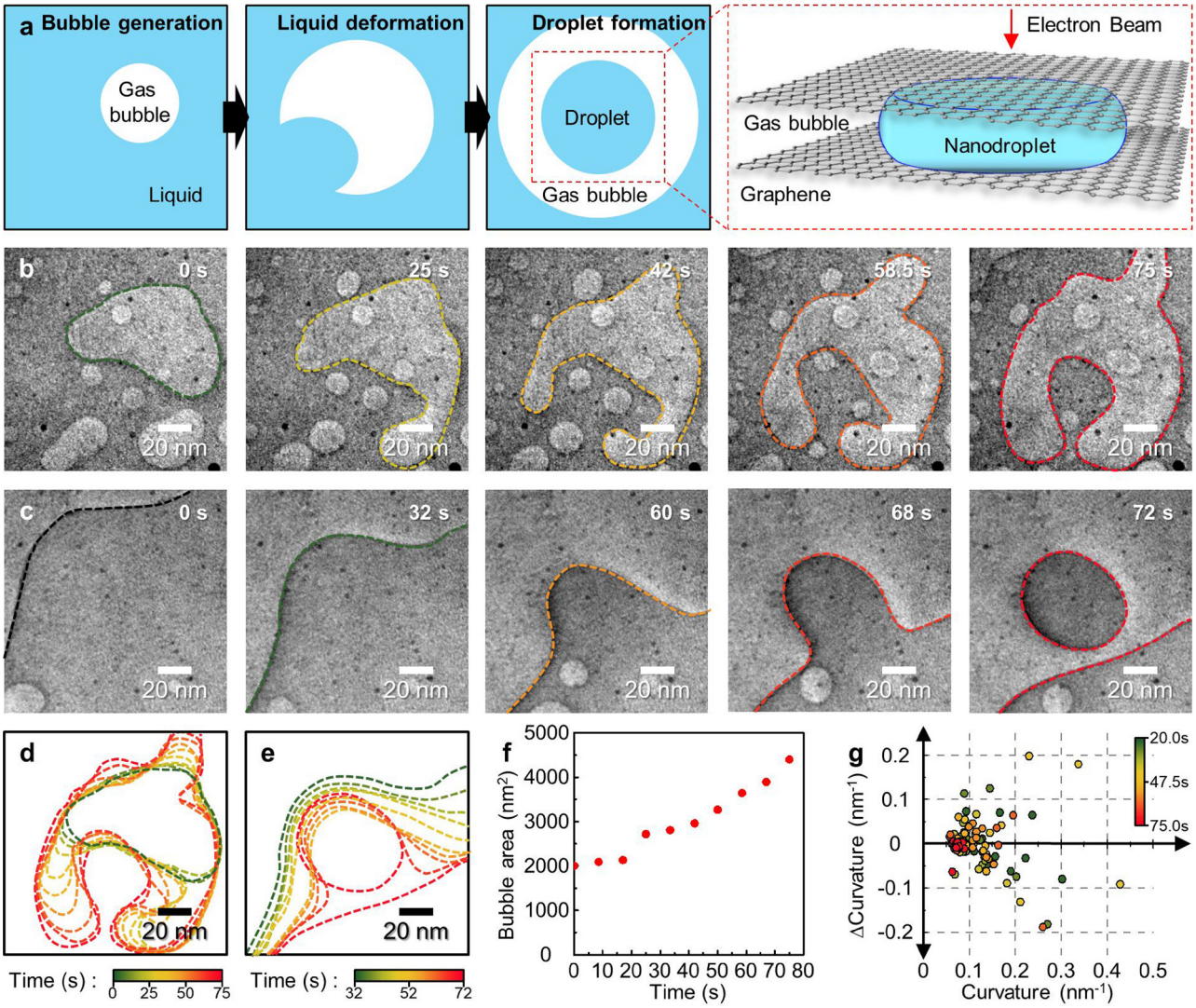

Fig. 1. Liquid deformation and nanodroplet formation in graphene liquid cells. (a) Schematics illustrating the deformation of liquid and the formation of aqueous nanodroplets between graphene sheets under the electron beam. (b,c) *In situ* TEM images showing the deformation of liquid and the formation of nanodroplets. The boundaries at the liquid-gas interface are highlighted by dashed lines. The corresponding movies are displayed in Movie S1 and Movie S2, respectively. (d,e) Contour plots of the liquid boundaries. (f) Plot of the bubble area acquired from the dashed lines in Movie S1 as a function of the measurement time. (g) Graph showing the changes in the curvature of liquid boundaries in the next time frame of *in situ* TEM imaging depending on the curvature. The data are acquired from the selected part of Movie S1, which is shown in Fig. S1.

additional gases under electron beam exposure. Fig. 1(f) displays the sizes of the bubbles in Movie S1 as a function of time, showing bubble growth (Fig. 1(a)). Since bubbles in graphene liquid cells are known to be trapped on the graphene surface (*i.e.*, surface bubbles), rather than free bubbles in bulk solution (Shin et al., 2015), it is not a surprise that they exist in non-spherical shapes. Local inhomogeneity of the graphene surface from defects, topological variations or partial bending/folding of graphene on the holey carbon substrate might influence the non-spherical shape of the bubbles. The growth of gas bubbles can generate liquid-gas interfaces with high curvature. Interestingly, *in situ* TEM movies show that the liquid-gas interface fluctuates, and the degree of fluctuation varies according to the curvature. Specifically, the local curvature is analyzed in the selected region of Movie S1 in the time range of 20 − 75 s (Fig. S1). Fig. 1(g) presents the change of local curvature in the next image frames according to the local curvature in the image of the previous frame. The change of the local curvature increases as the local curvature becomes larger, implying that local boundaries with higher curvature tend to deform more. With the synergetic effect of the bubble growth and the interface fluctuations, the liquid forms highly deformed shapes. In some cases, this results in the formation of liquid nanodroplets in the interior of surface nanobubbles (Fig. 1(a), (e) and Movie S2). The condensation of liquid vapor might also contribute to the formation of liquid droplets (Bhattacharya et al., 2014; Song et al., 2014), although it cannot be quantitatively estimated here. By forming the liquid nanodroplet, the gas bubble recovers low curvature interface and is stabilized. Many nanodroplets can be formed in similar measurement conditions (Fig. S2). These liquid nanodroplets can be easily distinguished from NaCl salt crystals that exhibit the crystalline lattice corresponding to the cubic crystal structure of NaCl (Figs. S3, S4 and Movie S3) (Zhou et al., 2015). This is supported by the electron energy loss spectroscopy (EELS) spectrum of the liquid droplet region that exhibits distinctive signals of O K-edge, while that of dried area shows almost no signal at the same measurement condition (Fig. S5).

The electron dose rate affects the degree of the fluctuations of the liquid (Movie S4). The morphological fluctuation of the liquid becomes more severe with increased electron dose rate (about 400 $e^{-}/Å^{2}s$, which is more than twice compared to Movie S1 and S2). A series of representative TEM images, from the early stages of Movie S4, are displayed in Fig. 2(a). In this case, the highlighted liquid inside the

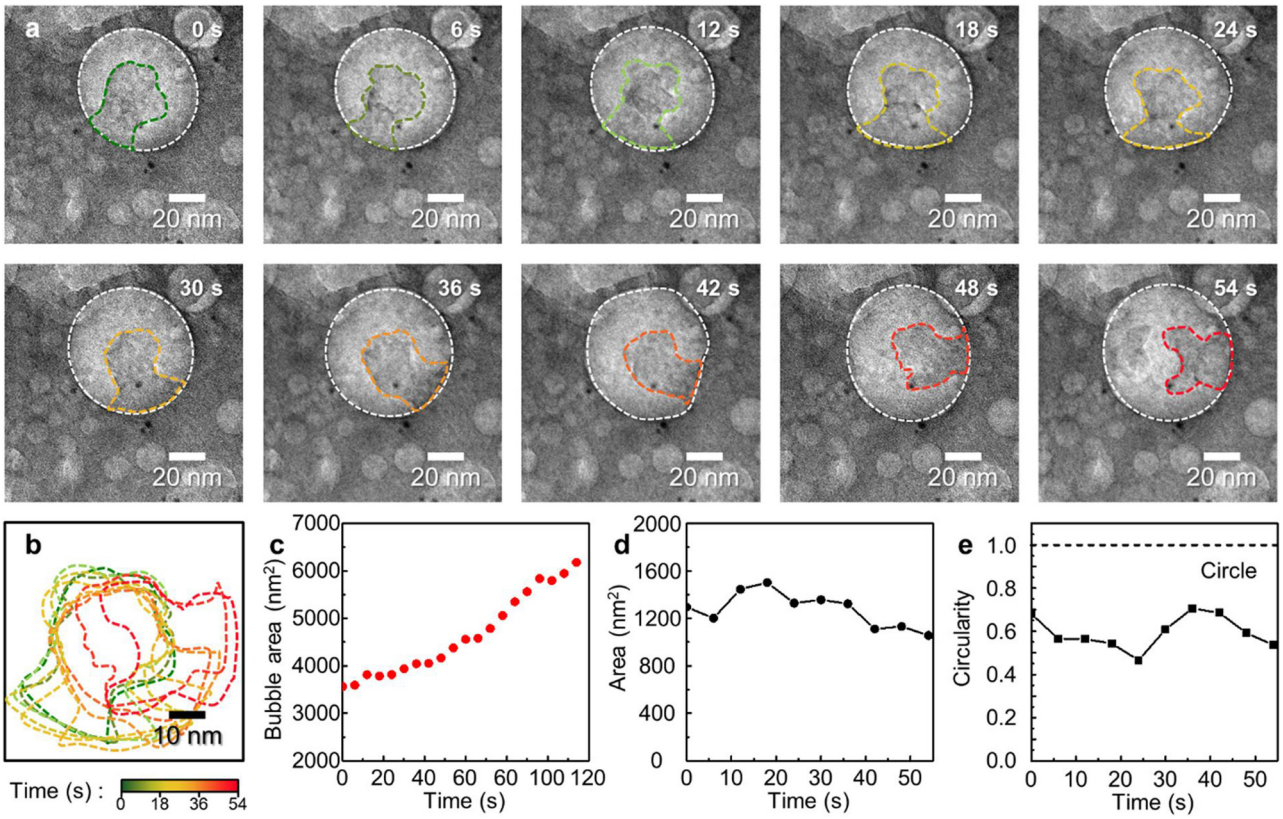

Fig. 2. Deformation of the liquid under the strong electron beam. (a) A time-series of *in situ* TEM images showing the liquid deformation under the strong electron beam (400 $e^{-}/Å^{2}$·s). The colored and the white dashed lines highlight the deformed liquid and gas bubbles. The images are extracted from Movie S4. (b) A contour plot of the liquid boundaries. (c) Plot of the bubble area acquired from the white dashed lines as a function of the measurement time. (d,e) Plots showing the area (d) and the circularity (e) of the deformed liquid part (highlighted by the color dashed lines in panel a) as a function of time.

bubble keeps attached to the outer liquid with the fast oscillating interfaces. The possible effect of the increasing dose rate on the morphology changes is discussed in details in Section 3.2. The contours of the highlighted liquid domain are shown in Fig. 2(b). As shown in Fig. 2(c), the size of the gas bubble keeps growing during the measurement of Movie S4, while its overall shape remains circular. The time-dependent projected area and the circularity of the highlighted liquid domain is plotted in Fig. 2(d) and (e), respectively. The projected area changes with the passage of time, which can be attributed to the significant morphology fluctuation of the liquid during the measurement and/or mass transport between the liquid domain and the liquid in the outer region.

3.2. Motion and fluctuations of nanodroplet interfaces

Another interesting feature is the dynamic behavior of the liquid droplets after their formation in the interior of a gas bubble. For example, in the mid-and-late part (68 − 86 s) of Movie S4 (displayed in Fig. 3(a)), as the experiment proceeds, the highly deformed liquid part is finally detached from the outer liquid and forms the liquid droplet in the interior of the gas bubble. TEM images of this liquid nanodroplet clearly show two boundaries, which can be attributed to the boundaries either formed by the liquid-gas interface contacting with graphene windows or maximum lateral size of the droplet. Schematics showing the cross section of the droplet is illustrated in Fig. S6 for two possible models: the cylinder and the (hemi-)sphere model. The two boundaries are highlighted as red and blue dashed lines in Fig. 3(a) and their contour plots are shown in Fig. 3(b). At first glance, the nanodroplet is almost fixed in their position while its boundaries are fluctuating under the beam exposure. Fig. 3(c) presents the area of the red and blue boundaries according to the time, showing consistent values during the measurement. This implies that the droplet is in the pseudo-steady state when it is detached from the outer liquid. Fig. 3(d) and (e) show the displacement in the center of the mass of the nanodroplet compared to that observed in the TEM image corresponding to the measurement time of 68 s, which confirms that there is almost no translational motion. The nanodroplets are almost pinned in their position, which is different from the previous study showing a huge slip movement of nanodroplets on the hydrophilic surface of SiN_x (Mirsaidov et al., 2012). This pinning can be regarded as the suppressed translational motion of the droplet on the hydrophobic surface, which is discussed in details in Section 3.3. In addition, there might be defects in the graphene making the area hydrophilic to pin the droplets. The graphene can react with hydroxyl radicals (Radich and Kamat, 2013; Qiu et al., 2014) which is one of the major products of water radiolysis under electron beam exposure (Woehl and Abellan, 2017), and the resulting products of graphene oxidation would be hydrophilic. Thus, as graphene is irradiated in the presence of water, the hydrophilic defects form and/or become more significant, which finally be able to pin the droplet. The circularity of the droplet is estimated for the red and blue boundaries (Fig. 3(f)), which is also consistent with the irregular and fluctuating shapes. Under the prolonged exposure of the electron beam, liquid droplets can be reattached to outer liquid (Movie S4), or merged into the outer liquid when gas bubbles disappear (Movie S5).

All together, the above results reveal that the nanodroplets (or liquid) exhibit fluctuating non-spherical irregular shapes under the electron beam. We have considered experimental factors that can induce the deformation of the liquid-gas interfaces. First of all, the electron beam induced heat effect is examined (Chen et al., 2018). Heating by the electron beam is not critical in microfabricated liquid cells with SiN_x windows (Mirsaidov et al., 2012; Loh et al., 2017). For graphene liquid cells, the liquid thickness is thinner than that in the

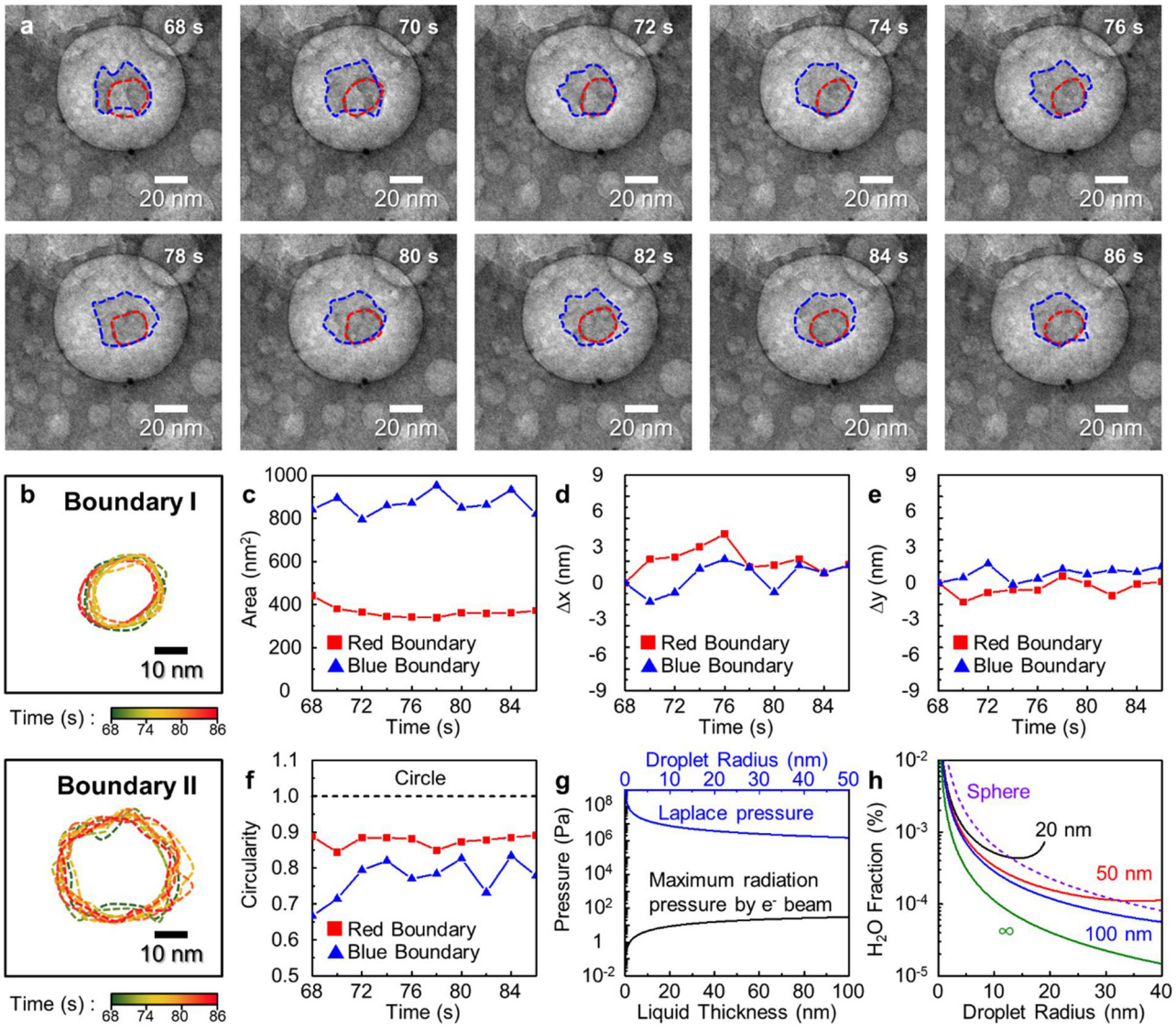

Fig. 3. Motion and shape evolution of the nanodroplet. (a) A time-series of *in situ* TEM images showing the motion and shape evolution of the aqueous nanodroplet. The red and blue dashed lines highlight the two liquid boundaries formed by contacting top and bottom graphene sheets. The images are extracted from Movie S4. (b) Contour plots of the liquid boundaries. Plots I and II are corresponding to red and blue boundaries of panel a, respectively. (c–f) Plots of the area (c), the displacement in the center of the mass (d,e), and circularity (f) of the liquid droplet as a function of the time. The values are acquired from red and blue boundaries in panel a. (g) Comparison of the Laplace pressure of the droplets and the maximum radiation pressure by the electron beam. (h) The critical fraction of charged water molecules, which is required for the electrostatic energy to exceed the surface energy, as a function of the droplet radius. The solid lines and the orange dashed line represent the cylinder model for different bubble radii and the sphere model, respectively (For interpretation of the references to colour in this figure legend, the reader is referred to the web version of this article).

microfabricated liquid cells and the thermal conductivity of the graphene (Balandin et al., 2008) is superior to SiN_x. In addition, the electron dose rate in our experiment is quite low ($100 - 400\ e^-/Å^2 s$). Consequently, heating effects are negligible in graphene liquid cells. Secondly, we have checked whether the radiation pressure can exceed Laplace pressure of the droplets, or not. The Laplace pressure is determined from the Young-Laplace equation as follows:

$$P_{Laplace} \equiv P_{inside} - P_{outside} = \gamma\left(\frac{1}{R_1} + \frac{1}{R_2}\right) \quad (1)$$

where γ is the liquid surface tension (0.075 N/m, Nayar et al., 2014), and R_1 and R_2 are the characteristic radii of the liquid: R_1 is the radius of the droplet, and $1/R_2$ can be regarded as 0 because of the flat surface of the graphene/nanodroplet interfaces. On the other hand, the radiation pressure of the electron beam can be expressed by the following equation according to the previous study (Mirsaidov et al., 2012):

$$P_{Rad} = \frac{N_{total}}{A\Delta t}\left(1-\exp\left(-\frac{l}{\lambda_{mean}}\right)\right)\sqrt{2m_e E}\,(1-\cos\theta) \quad (2)$$

where l is the thickness of the liquid and λ_{mean} is the mean free path of the 200 keV electron (Holtz et al., 2013). The maximum value is obtained when all the electrons are scattered completely backward (*i.e.*, $\theta = 180$). The result is plotted in Fig. 3(g) for the electron dose rate ($\frac{N_{total}}{A\Delta t}$) of 1000 $e^-/Å^2 \cdot s$, which is larger than our experiment condition. This analysis reveals that the calculated maximum radiation pressure is much smaller than the Laplace pressure, regardless of the liquid thickness or the droplet size. Thus, we can neglect the effects of radiation pressure.

Finally, we have examined whether the electrostatic energy ($E_{electrostatic}$) by charging can overcome the surface energy of the droplet (E_{surf}). The surface energy of the cylindrical droplets can be expressed by the eq. (3):

$$E_{surf} = \gamma A = 2\pi\gamma l R_{droplet} \quad (3)$$

where the surface area (A) of the droplet is approximately estimated from the cylindrical model (*i.e.*, l is the thickness of the liquid and $R_{droplet}$ is the radius of the droplet). The electrostatic energy of cylindrical droplets can be expressed by Eq. (4):

$$E_{electostatic} = \frac{q^2}{2C} = \frac{q^2}{4\pi\varepsilon_0 l}\ln\left(\frac{R_{bubble}}{R_{droplet}}\right) \quad (4)$$

where q is charge and ε_0 is permittivity (8.85×10^{-12} F/m). So, the electrostatic energy exceeds the surface energy of the droplet when the portion of the charged water molecules is higher than the critical point. Similarly, the critical fraction is also estimated for the sphere model by simply modifying Eq. (3) and (4). For both models, the calculated results are plotted in Fig. 3(h), demonstrating that very small amount ($< \sim 0.001\%$) of charged water molecules can possibly induce the deformation of liquid. This is consistent with the fact that the fluctuation becomes more severe with the increasing electron dose rate. It has been proposed that the electrostatic repulsion causes large slip movements of water nanodroplets on hydrophilic surfaces (Mirsaidov et al., 2012). Here, on the hydrophobic surface, this results in the severe surface fluctuation instead of the slip movement. In addition, we also suspect that bubble generation can also contribute to the interface fluctuation (Cho et al., 2017), although it cannot be quantitatively estimated because of its inhomogeneous generation (Grogan et al., 2014).

3.3. Impact of graphene wettability on the dynamic behavior of liquid

We investigate the impact of the surface wettability on the liquid dynamics. The change in total surface free energy (ΔG) of the cylindrical droplet due to the movement (ΔR) can be expressed by Eq. (5):

$$\Delta G \approx \left(\frac{dG}{dR}\right)_{\Delta R=0}\Delta R + \frac{1}{2}\left(\frac{d^2G}{dR^2}\right)_{\Delta R=0}\Delta R^2 = 2\pi(\gamma_{LS}-\gamma_{SG})\Delta R^2 \quad (5)$$

where the total surface free energy, $G(R_{droplet}) = 2(\gamma_{LS}-\gamma_{SG})\pi {R_{droplet}}^2 + 2\gamma\pi l R_{droplet}$ and $\left(\frac{dG}{dR}\right)_{\Delta R=0} = 0$ (Shanahan, 1995) (γ_{LS} and γ_{SG} are surface energy density at liquid-solid and solid-gas interface, respectively). Thus, the step movement can be expressed according to Eq. (6):

$$\Delta R = \sqrt{\frac{\Delta G}{2\pi(\gamma_{LS}-\gamma_{SG})}} \quad (6)$$

By applying the macroscopic relation of contact angle and surface tension, $cos\theta_c = (\gamma_{SG}-\gamma_{LS})/\gamma$, and by substituting the energy barrier as adhesion energy, $E_{ad} \approx 2 \times \pi R^2\gamma(1 + cos\theta_c)$ (Zisman, 1964), we can obtain the calculated movement length of the interface as a function of the contact angle (Fig. 4(a)). The calculation result for the hemisphere model is also displayed in Fig. 4(a). For both models, the values are decreasing with increasing contact angle and in the range of a few nanometer scales, which is about one order of magnitude smaller than the slip step length of water nanodroplets on the hydrophilic substrate reported in the previous study (Mirsaidov et al., 2012). This small step length is consistent with our observation that liquids fluctuate rather than slip.

To understand the significance of the surface energy on the dynamics of liquids on graphene, we compare the previous results with the dynamic behavior of the nanoscale liquid between the graphene sheets with hydrophilic surfaces. It is noted that the surface modification of graphene liquid cells has not been well established previously, so it is important to develop appropriate protocols for the fabrication of hydrophilic graphene liquid cells. Here, we utilize ultraviolet-ozone (UVO) treatment on graphene-coated grids. It has been recently demonstrated that UVO treatment induces the attachment of oxygen atoms onto graphene monolayers without significant lattice distortion, while other methods such as the oxygen plasma treatment inevitably introduce topological defects during the surface modification (Ryu et al., 2017). The graphene-coated grids with various UVO treatment times are characterized by Raman spectroscopy. Fig. 4(b) shows the Raman spectra of the graphene-coated grids with the different UVO exposure time from 0 s to 600 s. The characteristic peaks (D $\sim$1350 cm^{-1}, G $\sim$1700 cm^{-1}, and 2D bands $\sim$2700 cm^{-1}) of multilayer graphene are clearly detected for all the samples except the one with the longest exposure time of 600 s (Ferrari, 2007; Malard et al., 2009). This implies that the overall structure of the graphene is well preserved after the UVO treatment with the controlled time exposure. The relative intensity (I_{2D}/I_G) between G and 2D bands, which is correlated with the lattice distortion or defect of the graphene, is decreasing with the increasing exposure time. This can be attributed to the surface oxidation of graphene by the UVO treatment.

To determine the optimum UVO treatment condition, we measured the contact angle of the pure water on the graphene-coated grids with various exposure times (Fig. S7) and the result is summarized in Fig. 4(c). The contact angles dramatically decrease with the exposure time up to 150 s and are within measurement error for the samples with the treatment time of 150 s and 300 s. These results suggest the trend qualitatively on the modifications of the surface wettability. It should be noted that the acquired values of the macroscale contact angle cannot be directly applied for nanoscale liquids and their absolute values are not quantitatively meaningful, because they can be significantly affected by various factors such as the volume of liquid and surface morphology (Zhu et al., 2018). For example, the estimated value for the untreated graphene-coated grid ($\sim$102°) is smaller than the most widely accepted literature value for water on graphene (127°, Wang et al., 2009). The result unambiguously confirms that the UVO treatment can effectively modify the wettability of graphene grids from the hydrophobic to hydrophilic state within 150 s. Consequently, we selected the UVO treatment time of 150 s for the fabrication of liquid cells.

Finally, we have fabricated the graphene liquid cells using the surface treated graphene-coated grids. For the comparison experiments, all the measurement conditions are almost identical to the other *in situ* TEM experiments conducted in this study, except the use of the UVO treated girds. The results are presented in Fig. 4(d), (e) and Movie S6. The formation of a gas bubble is clearly observed, which directly confirms that liquid is well encapsulated in the UVO treated graphene liquid cells. This supports that the UVO treatment is not destructive, and thus, appropriate for the surface modification of graphene liquid cells. We can observe some different features in the liquid dynamics. The local fluctuation of the liquid-gas interface is observed, which is similar to the experiments with hydrophobic graphene. But the deformation of the liquid-gas interface can easily recover back to its low curvature state. Thus, the generation of liquid droplets is not observed in this comparison experiment. The smooth and fast translational motion of gas bubbles in the liquid cells is observed, which contrasts with the almost fixed position of surface bubbles in the previous observation. The spherical shape and fast translational motion are characteristics of non-surface free bubbles, which can be attributed to result of the enhanced wettability of the UVO treated graphene.

4. Conclusions

In summary, we have studied the dynamic behavior of aqueous liquid encapsulated between two graphene nanosheets using *in situ* TEM. The morphology of liquid can change under electron beam exposure, which can be attributed to the bubble growth and the interface fluctuations. This often leads to the formation of liquid nanodroplets that can exhibit morphological changes under the electron beam. We suggest that the electrostatic repulsion can cause the interfacial fluctuations of the liquid. In addition, the dynamic behavior of liquid can be controlled by the modification of the surface wettability of graphene liquid cells. Currently, there are still many challenges in order to fully

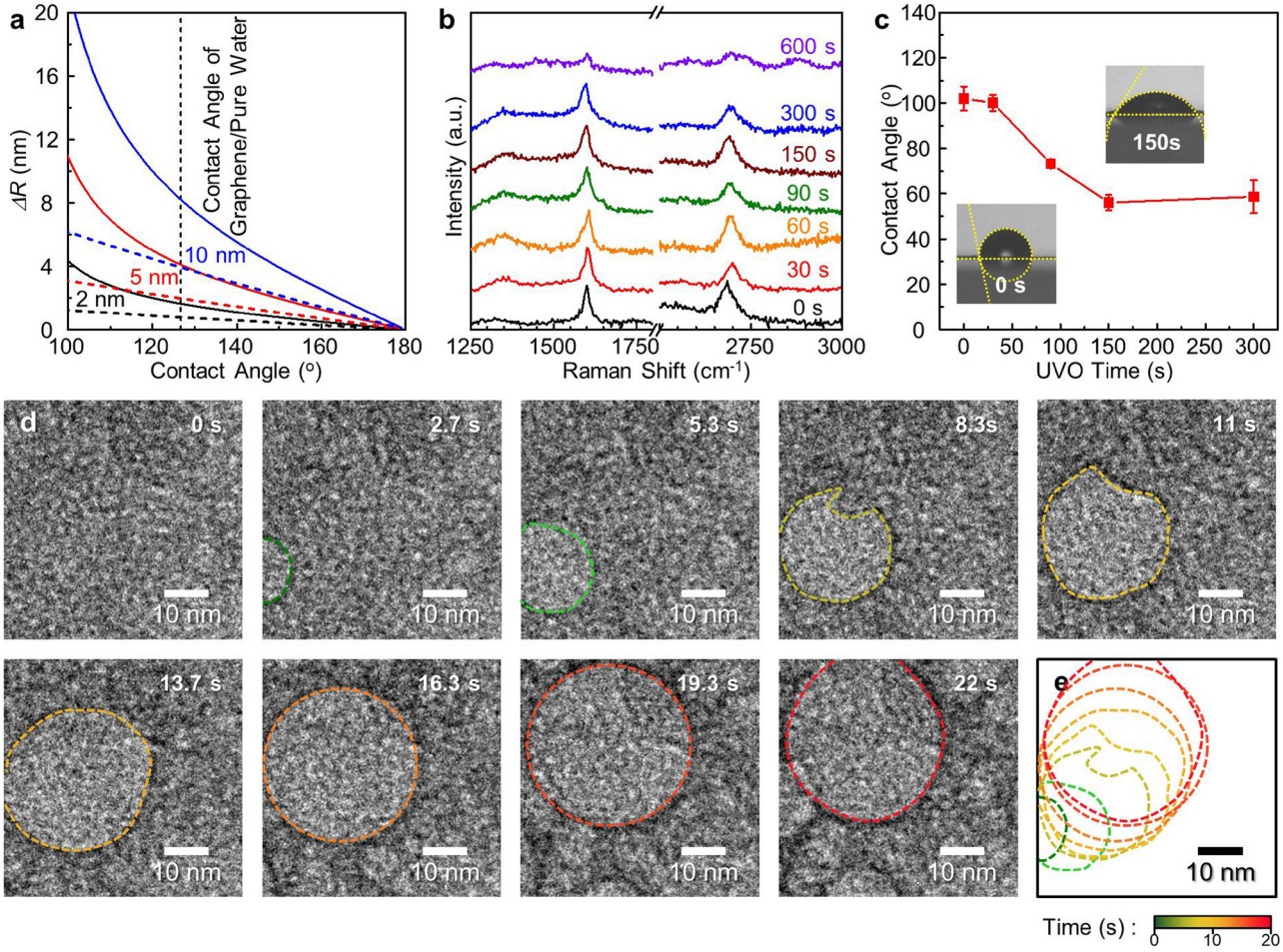

Fig. 4. Experiment with a hydrophilic graphene liquid cell for comparison. (a) The calculated step movement lengths of nanodroplets with different droplet radii (2, 5, and 10 nm) according to the contact angle. The solid and dashed lines represent the cylinder model and the hemisphere model. (b) Raman spectra of graphene according to the UVO treatment time. (c) Macroscopic contact angles of pure water on the graphene-coated grids as a function of the UVO treatment time. The insets display representative photograph images acquired from non-treated and UVO treated (150 s) graphene-coated grids. (d) A time-series of *in situ* TEM images showing dynamic behaviors of the liquid in the graphene liquid cell after surface treatment. The images are extracted from Movie S6. (e) A contour plot of the liquid-gas boundaries.

understand the liquid dynamics of liquid cell TEM. For example, it is difficult to estimate the exact liquid thickness during liquid cell experiments (Holtz et al., 2013) and there exist many unexplored chemical effects (such as radical scavenging effect of graphene (Cho et al., 2017)) that need to be addressed in the future works. Nevertheless, our study provides some valuable information for investigating liquid samples in graphene liquid cells using TEM. It also opens up new opportunities for studying liquids in confined conditions.

Acknowledgements

This work was funded by U.S. Department of Energy, Office of Science, Office of Basic Energy Sciences, Materials Sciences and Engineering Division under Contract No. DE-AC02-05-CH11231 within the insitu TEM program (KC22ZH). Work at the Molecular Foundry was supported by the Office of Science, Office of Basic Energy Sciences, of the U.S. Department of Energy under Contract No. DE-AC02-05CH11231.

Appendix A. Supplementary data

Supplementary material related to this article can be found, in the online version, at doi:https://doi.org/10.1016/j.micron.2018.09.009.

References

Abellan, P., Mehdi, B.L., Parent, L.R., Gu, M., Park, C., Xu, W., Zhang, Y., Arslan, I., Zhang, J.-G., Wang, C.-M., Evans, J.E., Browning, N.D., 2014. Probing the degradation mechanisms in electrolyte solutions for Li-ion batteries by in situ transmission electron microscopy. Nano Lett. 14, 1293–1299.
Algara-Siller, G., Lehtinen, O., Wang, F.C., Nair, R.R., Kaiser, U., Wu, H.A., Geim, A.K., Grigorieva, I.V., 2015. Square ice in graphene nanocapillaries. Nature 519, 443–445.
Balandin, A.A., Ghosh, S., Bao, W.Z., Calizo, I., Teweldebrhan, D., Miao, F., Lau, C.N., 2008. Superior thermal conductivity of single-layer graphene. Nano Lett. 8, 902–907.
Bhattacharya, D., Bosman, M., Mokkapati, V.R.S.S., Leong, F.Y., Mirsaidov, M., 2014. Nucleation dynamics of water nanodroplets. Microsc. Microanal. 20, 407–415.
Chen, Q., Smith, J.M., Park, J., Kim, K., Ho, D., Rasool, H.I., Zettl, A., Alivisatos, A.P., 2013. 3D motion of DNA-Au nanoconjugates in graphene liquid cell electron microscopy. Nano Lett. 13, 4556–4561.
Chen, J., Schusteritsch, G., Pickard, C.J., Salzmann, C.G., Michaelides, A., 2016. Two dimensional ice from first principles: structures and phase transitions. Phys. Rev. Lett. 116, 025501.
Chen, L., Wang, Y., Zhang, Z., 2018. Temperature distribution of wedge-shaped specimen in TEM. Micron 110, 46–49.
Cho, H., Jones, M.R., Nguyen, S.C., Hauwiller, M.R., Zettl, A., Alivisatos, A.P., 2017. The use of graphene and its derivatives for liquid-phase transmission electron microscopy of radiation-sensitive specimens. Nano Lett. 17, 414–420.
Choi, M.K., Park, I., Kim, D.C., Joh, E., Park, O.K., Kim, J., Kim, M., Choi, C., Yang, J., Cho, K.W., Hwang, J.-H., Nam, J.-M., Hyeon, T., Kim, J.H., Kim, D.-H., 2015. Thermally controlled, patterned graphene transfer printing for transparent and wearable electronic/optoelectronic system. Adv. Funct. Mater. 25, 7109–7118.
Cicero, G., Grossman, J.C., Schwegler, E., Gygi, F., Galli, G., 2008. Water confined in nanotubes and between graphene sheets: a first principle study. J. Am. Chem. Soc. 130, 1871–1878.
Cohen-Tanugi, D., Lin, L.-C., Grossman, J.C., 2016. Multilayer nanoporous graphene membranes for water desalination. Nano Lett. 16, 1027–1033.
Dahmke, I.N., Verch, A., Hermannsdorfer, J., Peckys, D.B., Weatherup, R.S., Hofmann, S.,

de Jonge, N., 2017. Graphene liquid enclosure for single-molecule analysis of membrane proteins in whole cells using electron microscopy. ACS Nano 11, 11108–11117.
de Jonge, N., 2018. Theory of the spatial resolution of (scanning) transmission electron microscopy in liquid water or ice layers. Ultramicroscopy 187, 113–125.
de Jonge, N., Ross, F.M., 2011. Electron microscopy of specimens in liquid. Nat. Nanotechnol. 6, 695–704.
De Yoreo, J.J., Sommerdijk, N.A.J.M., 2016. Investigating materials formation with liquid-phase and cryogenic TEM. Nat. Rev. Mater. 1, 16035.
Dollekamp, E., Bampoulis, P., Faasen, D.P., Zandvliet, H.J.W., Kooij, E.S., 2017. Charge induced dynamics of water in a graphene − mica slit pore. Langmuir 33, 11977–11985.
Ferrari, A.C., 2007. Raman spectroscopy of graphene and graphite: Disorder, electron–phonon coupling, doping and nonadiabatic effects. Solid State Commun. 143, 47–57.
Geim, A.K., Grigorieva, I.V., 2013. Van der Waals heterostructures. Nature 499, 419–425.
Grogan, J.M., Schneider, N.M., Ross, F.M., Bau, H.H., 2014. Bubble and pattern formation in liquid induced by an electron beam. Nano Lett. 14, 359–364.
Gu, M., Parent, L.R., Mehdi, B.L., Unocic, R.R., McDowell, M.T., Sacci, R.L., Xu, W., Connell, J.G., Xu, P., Abellan, P., Chen, X., Zhang, Y., Perea, D.E., Evans, J.E., Lauhon, L.J., Zhang, J.-G., Liu, J., Browning, N.D., Cui, Y., Arslan, I., Wang, C.-M., 2013. Demonstration of an electrochemical liquid cell for operando transmission electron microscopy observation of the lithiation/delithiation behavior of Si nanowire battery anodes. Nano Lett. 13, 6106–6112.
Holt, J.K., Park, H.G., Wang, Y., Stadermann, M., Artyukhin, A.B., Grigoropoulos, C.P., Noy, A., Bakajin, O., 2006. Fast mass transport through sub-2-nanometer carbon nanotubes. Science 312, 1034–1037.
Holtz, M.E., Yu, Y., Gao, J., Abruña, H.D., Muller, D.A., 2013. In situ electron energy-loss spectroscopy in liquids. Microsc. Microanal. 19, 1027–1035.
Jiang, Y., Zhu, G., Dong, G., Ling, F., Zhang, H., Yuan, J., Zhang, Z., Jin, C., 2017. Probing the oxidative etching induced dissolution of palladium nanocrystals in solution by liquid cell transmission electron microscopy. Micron 97, 22–28.
Kelly, D., Zhou, M., Clark, N., Hamer, M.J., Lewis, E.A., Rakowski, A.M., Haigh, S.J., Gorbachev, R.V., 2018. Nanometer resolution elemental mapping in graphene-based TEM liquid cells. Nano Lett. 18, 1168–1174.
Kim, J.-Y., Yang, J., Yu, J.H., Baek, W., Lee, C.-H., Son, H.J., Hyeon, T., Ko, M.J., 2015. Highly efficient copper–indium–selenide quantum dot solar cells: Suppression of carrier recombination by controlled ZnS overlayers. ACS Nano 9, 11286–11295.
Kim, B.H., Yang, J., Lee, D., Choi, B.K., Hyeon, T., Park, J., 2018. Liquid-phase transmission electron microscopy for studying colloidal inorganic nanoparticles. Adv. Mater. 30, 1703316.
Kolesnikov, A.I., Zanotti, J.-M., Loong, C.-K., Thiyagarajan, P., Moravsky, A.P., Loutfy, R.O., Burnham, C.J., 2004. Anomalously soft dynamics of water in a nanotube: a revelation of nanoscale confinement. Phys. Rev. Lett. 93, 035503.
Lee, W.C., Kim, K., Park, J., Koo, J., Jeong, H.Y., Lee, H., Weitz, D.A., Zettl, A., Takeuchi, S., 2015. Graphene-templated directional growth of an inorganic nanowire. Nat. Nanotechnol. 10, 423–428.
Lee, J., Yang, J., Kwon, S.G., Hyeon, T., 2016. Nonclassical nucleation and growth of inorganic nanoparticles. Nat. Rev. Mater. 1, 16034.
Leong, F.Y., Mirsaidov, U.M., Matsudaria, P., Mahadevan, L., 2014. Dynamics of a nanodroplet under a transmission electron microscope. Phys. Fluids 26, 012003.
Li, Q., Song, J., Besenbacher, F., Dong, M., 2014. Two-dimensional material confined water. Acc. Chem. Res. 48, 119–127.
Liao, H.-G., Zherebetskyy, D., Xin, H., Czarnik, C., Ercius, P., Elmlund, H., Pan, M., Wang, L.-W., Zheng, H., 2014. Facet development during platinum nanocube growth. Science 345, 916–919.
Liao, H.-G., Zheng, H., 2016. Liquid cell transmission electron microscopy. Ann. Rev. Phys. Chem. 67, 719–747.
Loh, N.D., Sen, S., Bosman, M., Tan, S.F., Zhong, J., Nijhuis, C., Kral, P., Matsudaira, P., Mirsaidov, U., 2017. Multi-step nucleation of nanocrystals. Nat. Chem. 9, 77–82.
Lucent, D., Vishal, V., Pande, V.S., 2007. Protein folding under confinement: a role for solvent. Proc. Natl. Acad. Sci. U. S. A. 104, 10430–10434.
Luo, B., Smith, J.W., Ou, Z., Chen, Q., 2017. Quantifying the self-assembly behavior of anisotropic nanoparticles using liquid-phase transmission electron microscopy. Acc. Chem. Res. 50, 1125–1133.
Malard, L.M., Pimenta, M.A., Dersselhaus, G., Dersselhaus, M.S., 2009. Raman spectroscopy in graphene. Phys. Rep. 473, 51–87.
Mirsaidov, U.M., Zheng, H., Bhattacharya, D., Casana, Y., Matsudaira, P., 2012. Direct observation of stick-slip movements of water nanodroplets induced by an electron beam. Proc. Natl. Acad. Sci. U. S. A. 109, 7187–7190.
Nayar, K.G., Panchanathan, D., McKinley, G.H., Lienhard, J.H., 2014. Surface tension of seawater. J. Phys. Chem. Ref. Data 43, 43103.
Nielsen, M.H., Aloni, S., De Yoreo, J.J., 2014. In situ TEM imaging of $CaCO_3$ nucleation reveals coexistence of direct and indirect pathways. Science 345, 1158–1162.
Niu, K.Y., Park, J., Zheng, H., Alivisatos, A.P., 2014. Revealing bismuth oxide hollow nanoparticle formation by the Kirkendall effect. Nano Lett. 13, 5715–5719.
Niu, K.Y., Frolov, T., Xin, H.L., Wang, J., Asta, M., Zheng, H., 2015. Bubble nucleation and migration in a lead-Iron hydroxide core-shell nanoparticle. Proc. Natl. Acad. Sci. U. S. A. 112, 12928–12932.
Novoselov, K.S., Mishchenko, A., Carvalho, A., Castro Neto, A.H., 2016. 2D materials and van der Waals heterostructures. Science (80-) 353, aac9439.
Park, J., Park, H., Ercius, P., Pegoraro, A.F., Xu, C., Kim, J.W., Han, S.H., Weitz, D.A., 2015a. Direct observation of wet biological samples by graphene liquid cell transmission electron microscopy. Nano Lett. 15, 4737–4744.
Park, J., Elmlund, H., Ercius, P., Yuk, J.M., Limmer, D.T., Chen, Q., Kim, K., Han, S.H., Weitz, D.A., Zettl, A., Alivisatos, A.P., 2015b. 3D structure of individual nanocrystals in solution by electron microscopy. Science 2015 (349), 290–295.
Pestana, L.R., Felberg, L.E., Head-Gordon, T., 2018. Coexistence of multilayered phases of confined water: the importance of flexible confining surfaces. ACS Nano 12, 448–454.
Powers, A.S., Liao, H.-G., Raja, S.N., Bronstein, N.D., Alivisatos, A.P., Zheng, H., 2016. Tracking nanoparticle diffusion and interaction during self-assembly in a liquid cell. Nano Lett. 17, 15–20.
Qiu, Y., Wang, Z., Owens, A.C.E., Kulaots, I., Chen, Y., Kane, A.B., Hurt, R.H., 2014. Antioxidant chemistry of graphene-based materials and its role in oxidation protection technology. Nanoscale 6, 11744–11755.
Radich, J.G., Kamat, P.V., 2013. Making graphene holey. Gold-nanoparticle-mediated hydroxyl radical attack on reduced graphene oxide. ACS Nano 7, 5546–5557.
Regan, W., Alem, N., Alemán, B., Geng, B., Girit, C., Maserati, L., Wang, F., Crommie, M., Zettl, A., 2010. A direct transfer of layer-area graphene. Appl. Phys. Lett. 96, 113102.
Ross, F.M., 2015. Opportunities and challenges in liquid cell electron microscopy. Science 350, aaa9886.
Ryu, G.H., Lee, J., Kang, D., Jo, H.J., Shin, H.S., Lee, Z., 2017. Effects of dry oxidation treatments on monolayer graphene. 2D Mater. 4, 024011.
Schindelin, J., Arganda-Carreras, I., Frise, E., Kaynig, V., Longair, M., Pietzsch, T., Preibisch, S., Rueden, C., Saalfeld, S., Schmid, B., Tinevez, J.Y., White, D.J., Hartenstein, V., Eliceiri, K., Tomancak, P., Cardona, A., 2012. Fiji: an open-source platform for biological-image analysis. Nat. Methods 9, 676–682.
Schneider, N.M., Norton, M.M., Mendel, B.J., Grogan, J.M., Ross, F.M., Bau, H.H., 2014. Electron–water interactions and implications for liquid cell electron microscopy. J. Phys. Chem. C 118, 22373–22382.
Shanahan, M.E.R., 1995. Simple theory of “stick-slip” wetting hysteresis. Langmuir 11, 1041–1043.
Shin, D., Park, J.B., Kim, Y.-J., Kim, S.J., Kang, J.H., Lee, B., Cho, S.-P., Hong, B.H., Novoselov, K.S., 2015. Growth dynamics and gas transport mechanism of nanobubbles in graphene liquid cells. Nat. Commun. 6, 6068.
Song, Z., Xie, Z.-H., 2018. A literature review of in situ transmission electron microscopy technique in corrosion studies. Micron 112, 69–83.
Song, J., Li, Q., Wang, X., Li, J., Zhang, S., Kjems, J., Besenbacher, F., Dong, M., 2014. Evidence of Stranski-Krastanov growth at the initial stage of atmospheric water condensation. Nat. Commun. 5, 4837.
Stalder, A.F., Kulik, G., Sage, D., Barbieri, L., Hoffmann, P., 2006. Snake-based approach to accurate determination of both contact points and contact angles. Colloids Surf. A 286, 92–103.
Sutter, E., Jungjohann, K., Bliznakov, S., Courty, A., Maisonhaute, E., Tenney, S., Sutter, P., 2014. In situ liquid-cell electron microscopy of silver–palladium galvanic replacement reactions on silver nanoparticles. Nat. Commun. 5, 4946.
Sutter, P., Li, Y., Argyropoulos, C., Sutter, E., 2017. In situ electron microscopy of plasmon-mediated nanocrystal synthesis. J. Am. Chem. Soc. 139, 6771–6776.
Takaiwa, D., Hatano, I., Koga, K., Tanaka, H., 2008. Phase diagram of water in carbon nanotubes. Proc. Natl. Acad. Sci. U. S. A. 105, 39–43.
Tan, S.F., Chee, S.W., Lin, G., Mirsaidov, U., 2017. Direct observation of interaction between nanoparticles and their self-assembly in solution. Acc. Chem. Res. 50, 1303–1312.
Textor, M., de Jonge, N., 2018. Strategies for preparing graphene liquid cells for transmission electron microscopy. Nano Lett. 18, 3313–3321.
Wang, S., Zhang, Y., Abidi, N., Cabrales, L., 2009. Wettability and surface free energy of graphene films. Langmuir 25, 11078–11081.
Wang, S., Wang, X., Warner, J.H., 2015. All chemical vapor deposition growth of MoS_2:h-BN vertical van der Waals hetero structures. ACS Nano 9, 5246–5254.
Williamson, M.J., Tromp, R.M., Vereecken, P.M., Hull, R., Ross, F.M., 2003. Dynamic microscopy of nanoscale cluster growth at the solid-liquid interface. Nat. Mater. 2, 532–536.
Woehl, T.J., Abellan, P., 2017. Defining the radiation chemistry during liquid cell electron microscopy to enable visualization of nanomaterial growth and degradation dynamics. J. Microsc. 265, 135–147.
Woehl, T.J., Evans, J.E., Arslan, I., Ristenpart, W.D., Browning, N.D., 2012. Direct in situ determination of the mechanisms controlling nanoparticle nucleation and growth. ACS Nano 6, 8599–8610.
Yang, J., Kim, K., Lee, Y., Kim, K., Lee, W.C., Park, J., 2017. Self-organized growth and self-assembly of nanostructures on 2D materials. FlatChem 5, 50–68.
Yuk, J.M., Park, J., Ercius, P., Kim, K., Hellebusch, D.J., Crommie, M.F., Lee, J.Y., Zettl, A., Alivisatos, A.P., 2012. High-resolution EM of colloidal nanocrystal growth using graphene liquid cells. Science 336, 61–64.
Zeng, Z., Zheng, W., Zheng, H., 2017. Visualization of colloidal nanocrystal formation and electrode-electrolyte interfaces in liquids using TEM. Acc. Chem. Res. 50 1808-1807.
Zhang, Q., Yin, K., Dong, H., Zhou, Y., Tan, X., Yu, K., Hu, X., Xu, T., Zhu, C., Xia, W., Xu, F., Zheng, H., Sun, L., 2017. Electrically driven cation exchange for in situ fabrication of individual nanostructures. Nat. Commun. 8, 14889.
Zheng, H., Smith, R.K., Jun, Y.W., Kisielowski, C., Dahmen, U., Alivisatos, A.P., 2009. Observation of single colloidal platinum nanocrystal growth trajectories. Science 324, 1309–1312.
Zhou, W., Yin, K., Wang, C., Zhang, Y., Xu, T., Borisevich, A., Sun, L., Idrobo, J.C., Chisholm, M.F., Pantelides, S.T., Klie, R.F., Lupini, A.R., 2015. The observation of square ice in graphene questioned. Nature 528, E1–E2.
Zhou, Y., Powers, A.S., Zhang, X., Xu, T., Bustillo, K., Sun, L., Zheng, H., 2017. Growth and assembly of cobalt oxide nanoparticle rings at liquid nanodroplets with solid junction. Nanoscale 9, 13915–13921.
Zhu, Y., Durr, H., 2015. The future of electron microscopy. Phys. Today 68, 32–38.
Zhu, Z., Guo, H.K., Jiang, X.K., Chen, Y.C., Song, B., Zhu, Y.M., Zhuang, S.L., 2018. Reversible hydrophobicity–hydrophilicity transition modulated by surface curvature. J. Phys. Chem. Lett. 9, 2346–2352.
Zisman, W.A., 1964. Relation of the equilibrium contact angle to liquid and solid constitution. In: Fowkes, F.M. (Ed.), Contact Angle, Wettability, and Adhesion. American Chemical Society, Washington, DC, pp. 1–51.